

# The Stability of the Thermohaline Circulation in Global Warming Experiments

ANDREAS SCHMITTNER AND THOMAS F. STOCKER

*Climate and Environmental Physics, Physics Institute, University of Bern, Bern, Switzerland*

(Manuscript received 2 December 1997, in final form 12 June 1998)

## ABSTRACT

A simplified climate model of the coupled ocean–atmosphere system is used to perform extensive sensitivity studies concerning possible future climate change induced by anthropogenic greenhouse gas emissions. Supplemented with an active atmospheric hydrological cycle, experiments with different rates of CO<sub>2</sub> increase and different climate sensitivities are performed. The model exhibits a threshold value of atmospheric CO<sub>2</sub> concentration beyond which the North Atlantic Deep Water formation stops and never recovers. For a climate sensitivity that leads to an equilibrium warming of 3.6°C for a doubling of CO<sub>2</sub> and a rate of CO<sub>2</sub> increase of 1% yr<sup>−1</sup>, the threshold lies between 650 and 700 ppmv.

Moreover, it is shown that the stability of the thermohaline circulation depends on the rate of increase of greenhouse gases. For a slower increase of atmospheric pCO<sub>2</sub> the final amount that can be reached without a shutdown of the circulation is considerably higher. This rate-sensitive response is due to the uptake of heat and excess freshwater from the uppermost layers to the deep ocean.

The increased equator-to-pole freshwater transport in a warmer atmosphere is mainly responsible for the cessation of deep water formation in the North Atlantic. Another consequence of the enhanced latent heat transport is a stronger warming at high latitudes. A model version with fixed water vapor transport exhibits uniform warming at all latitudes. The inclusion of a simple parameterization of the ice-albedo feedback increases the model sensitivity and further decreases the pole-to-equator temperature difference in a greenhouse climate. The possible range of CO<sub>2</sub> threshold concentrations and its dependency on the rate of CO<sub>2</sub> increase, on the climate sensitivity, and on other model parameters are discussed.

## 1. Introduction

Human activities, like the emission of fossil fuels or changes in land use, increase the concentration of greenhouse gases in the atmosphere. Atmospheric CO<sub>2</sub>, for example, increased from a preindustrial concentration of about 280 ppmv (Neftel et al. 1988) to values of over 360 ppmv at the end of the 1990s (Keeling and Whorf 1994). Since it cannot be expected that the anthropogenic greenhouse gas emissions will be drastically reduced in the near future, many modeling studies have already been addressing the possible future consequences for the climate system. The Intergovernmental Panel on Climate Change (IPCC) recently summarized the main responses of current three-dimensional coupled ocean–atmosphere models to increased atmospheric CO<sub>2</sub> concentrations (Houghton et al. 1996). The range of the predicted global mean surface air temperature rise for a doubling of preindustrial CO<sub>2</sub> is between 2.1° and 4.6°C.

The purpose of this paper is to study possible impacts of global warming on the atmosphere–ocean system with a simplified coupled ocean–atmosphere climate model for the whole range of temperature changes reported by Houghton et al. (1996). We will investigate the existence and values of thresholds for major reorganizations in the climate system and focus particularly on the long-term behavior of the model.

The climate system has different stable equilibria as paleoclimatic records (Oeschger et al. 1984; Broecker et al. 1985; Broecker and Denton 1989) and modeling studies (Bryan 1986; Manabe and Stouffer 1988) indicate. Transitions between the different steady states can be caused by perturbations such as additional freshwater input into selected oceanic areas or variations of the solar energy input. Manabe et al. (1991) and Cubasch et al. (1992) showed with their three-dimensional coupled ocean–atmosphere models that global warming could increase the stability of the high-latitude ocean waters and therefore reduce the ocean's thermohaline circulation. Manabe and Stouffer (1993) found a threshold value for the collapse of the thermohaline circulation that is between two and four times the preindustrial CO<sub>2</sub> concentration of 280 ppmv. A reduction of deep ocean ventilation as well as the decreased CO<sub>2</sub> solubility of the warmer surface waters of the ocean will both reduce

*Corresponding author address:* Andreas Schmittner, Climate and Environmental Physics, Physics Institute, University of Bern, Sidlerstrasse 5, CH-3012 Bern, Switzerland.  
E-mail: schmittner@climate.unibe.ch

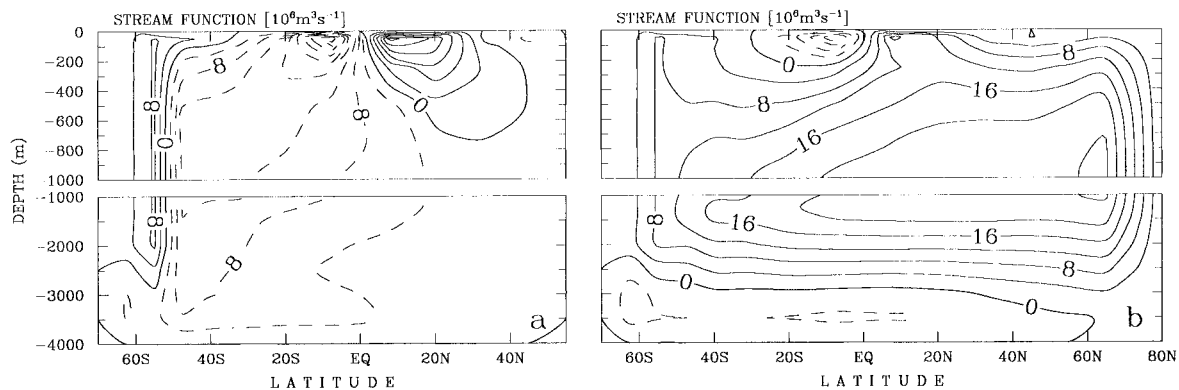


FIG. 1. Latitude–depth section of modeled meridional overturning streamfunction in the Pacific (a) and Atlantic (b) Oceans before the start of the global warming experiments. Deep water is formed in the Southern Ocean and in the North Atlantic. It is then slowly upwelling in the rest of the world's oceans (Indian Ocean not shown).

the  $\text{CO}_2$  uptake of the ocean, a positive feedback on atmospheric  $p\text{CO}_2$ .

Three-dimensional coupled ocean–atmosphere models are extremely expensive and take much computational time for integrations extending over many centuries; this precludes extensive sensitivity studies. Presently there are only very few such long-term integrations (Manabe and Stouffer 1994). The aim of the present study, recently summarized by Stocker and Schmittner (1997), is therefore to investigate the response of a simplified climate model on a long timescale (centuries to thousands of years). Special emphasis is put on the thermohaline circulation and extensive sensitivity studies will be performed to examine the parameter space with a focus on structurally different equilibria and the dynamics of the coupled atmosphere–ocean system, which are responsible for transitions between these equilibria.

The paper is organized as follows: section 2 explains the model that we use for these experiments, which are detailed in section 3; sensitivity studies are presented in section 4; and sections 5 and 6 give a discussion and the conclusions of our findings, respectively.

## 2. Model description

We use the zonally averaged three-basin ocean circulation model of Wright and Stocker (1991), which is coupled to a one-dimensional zonally and vertically averaged energy balance model (EBM) of the atmosphere (Stocker et al. 1992). The dynamics of the ocean model is based on the vorticity balance in a zonally averaged basin (Wright et al. 1998). It consists of three individual basins representing the Atlantic, the Pacific, and the Indian Oceans, which are connected by an Antarctic circumpolar channel. The model geometry is identical to that used by Stocker and Wright (1996) and includes a simple thermodynamic sea ice component (Wright and Stocker 1993); the seasonal cycle is neglected.

The ocean model is spun up from rest by relaxing

the surface values of temperature and salinity to the zonal and annual mean climatological data from Levitus (1982) with a restoring timescale of 50 days. A quasi-steady state is reached after 4000 yr of integration. After switching to mixed boundary conditions and further integration for 1000 yr the atmosphere component is coupled to the ocean model. Figure 1 shows the steady-state meridional overturning in the Atlantic and Pacific Oceans after 1000 yr of coupled integration, which is very close to the state before coupling. The present circulation is simulated well with deep water formation in the North Atlantic and in the Southern Ocean. Salinity and temperature distributions (not shown) are also in good agreement with modern zonally averaged observations (Levitus et al. 1994; Levitus and Boyer 1994).

The procedure of determination of various atmospheric model parameters is discussed in detail in Stocker et al. (1992). No atmospheric dynamics are incorporated in the EBM; instead the meridional atmospheric transport of sensible heat,

$$\mathbf{F} = -K_T \nabla T, \quad (1)$$

is parameterized as an eddy-diffusive process with a latitude-dependent eddy diffusion coefficient,  $K_T(\varphi)$ . Here  $T$  is the near-surface air temperature and  $\nabla$  is the gradient operator. This parameterization, or close relatives of it, has been used successfully in low-order climate models that have no representation of the dynamics in the atmosphere (e.g., Ghil 1985). For large spatial scales ( $>1000$  km) and long temporal scales ( $>6$  months) this simple parameterization is supported by data (Lorenz 1979).

In contrast to the meridional flux of sensible heat, which could vary in time in response to temperature changes, the meridional latent heat flux was kept fixed in previous model versions. A new formulation of the atmospheric part of the hydrological cycle, described in the following section, is included to overcome this weakness.

TABLE 1. Model parameters.

$K_T$	Eddy diffusivity for sensible heat	Range: Fig. 3
$K_q$	Eddy diffusivity for water vapor	Range: Fig. 3
$H_q$	Scale height for humidity	1800 m
$r$	Relative humidity	0.85
$L$	Latent heat of evaporation	$2.5 \cdot 10^6 \text{ J kg}^{-1}$
$\rho_A$	Surface air density	$1.225 \text{ kg m}^{-3}$
$a$	Radius of the earth	$6.371 \cdot 10^6 \text{ m}$
$S_o$	Ocean reference salinity	34.7
$\rho_o$	Ocean reference density	$1027.786 \text{ kg m}^{-3}$
$R_d$	Gas constant for dry air	$287 \text{ J kg}^{-1} \text{ K}^{-1}$
$T_0$	Reference temperature	273 K
$e_s(T_0)$	Reference pressure	611 Pa

### The hydrological cycle

A balance equation for the specific humidity  $q$  {kg (water vapor) [kg (moist air)]<sup>-1</sup>} can be formulated analogous to the equation for the temperature [Eq. (13) in Stocker et al. 1992]. Assuming stationarity ( $\partial/\partial t = 0$ ) the divergence of the latent heat flux must be balanced by the sources and sinks. This can be written as

$$\frac{\partial q}{\partial t} = -\nabla \cdot \mathbf{L} + E - P = 0, \quad (2)$$

where  $\mathbf{L}$  is the meridional flux of water vapor and  $E$  and  $P$  are the moisture changes due to evaporation and precipitation zonally averaged over the three ocean basins (Pacific, Atlantic, Indian):

$$E - P = \frac{1}{L\rho_A H_q} \sum_{n=1}^3 \frac{\Delta\Lambda_n}{2\pi} (E_n - P_n), \quad (3)$$

where  $E_n$  and  $P_n$  are latent heat fluxes due to evaporation and precipitation into basin  $n$  in  $\text{W m}^{-2}$ . Here  $\Delta\Lambda_n$  is the longitudinal angular width of basin  $n$ . The values for the scaling height for humidity  $H_q$  (Fanning and Weaver 1996), the surface air density  $\rho_A$ , and the latent heat of evaporation  $L$ , as well as other parameters, are given in Table 1.

In analogy to Eq. (1) the meridional flux of water vapor is taken proportional to the moisture gradient:

$$\mathbf{L} = -K_q \nabla q, \quad (4)$$

where  $K_q(\varphi)$  is a constant meridional eddy diffusivity depending on latitude  $\varphi$ . Following Chen et al. (1995) we assume a constant relative humidity  $r = q/q_s$ , where  $q_s$  is the saturation specific humidity, and we can set

$$\mathbf{L} = -K_q r \frac{\partial q_s}{\partial T} \nabla T. \quad (5)$$

The meridional flux of latent heat is now related to the temperature gradient, so that no prognostic calculation of the specific humidity is necessary.

The saturation specific humidity is a function of surface air temperature and air pressure  $p = 10^5 \text{ Pa}$  near the surface,

$$q_s = q_s(T, p) = \frac{0.622}{p} e_s, \quad (6)$$

where  $e_s$  is saturation water vapor pressure (see James 1994, 246) given by

$$e_s = e_s(T_0) \exp \left[ -0.622 \frac{L}{R_d} \left( \frac{1}{T} - \frac{1}{T_0} \right) \right]. \quad (7)$$

The values of the various parameters like the gas constant for dry air  $R_d$  or  $T_0$  and  $e_s(T_0)$  are given in Table 1. Since evaporation  $E = (\sum \Delta\Lambda_n E_n) / (2\pi L\rho_A H_q)$  is a known function of the near-surface air temperature  $T$  and the sea surface temperature (see Stocker et al. 1992), we can now diagnose the zonally averaged precipitation from Eq. (2):

$$P = E + \nabla \cdot \left( K_q r \frac{\partial q_s}{\partial T} \nabla T \right). \quad (8)$$

The one-dimensional form of Eq. (8) in spherical coordinates reads

$$P = E + \frac{1}{a \cos \varphi} \frac{\partial}{\partial \varphi} \left( \cos \varphi K_q r \frac{\partial q_s}{\partial T} \frac{\partial T}{\partial \varphi} \right), \quad (9)$$

where  $a$  is the radius of the earth.

From Eq. (8) or (9) and (3) it is clear that we can only determine the zonal mean precipitation  $P$ . Since we have no information on the zonal distribution of precipitation  $P$  on the individual ocean basins, we must make a closure assumption. The lack of information on a parameterization of the zonal distribution of precipitation forced us to make some ad hoc assumptions. Model experiments were performed for two different closures (P1 and P2) to examine the sensitivity of the model response due to different zonal distributions of precipitation.

- 1) As the standard closure (P1) we take the value  $P_n/P$ , which can be determined from the spinup of the ocean model, as a constant at any latitude. This means that the relative zonal distribution of precipitation into the different basins will not change. Figure 2 shows the normalized ratio  $P_n/P$  for the three basins.
- 2) The second closure (P2) is based on a split of the zonally averaged precipitation  $\bar{P}(t) = \bar{P}_0 + \bar{P}^*(t)$  into its value at the time of coupling  $\bar{P}_0$ , which is constant, and the time-dependent anomaly  $\bar{P}^*(t)$ . Here the overbar denotes the zonal mean precipitation  $\bar{P} = \sum_{n=1}^3 (\Delta\Lambda_n / 2\pi) P_n$  in  $\text{W m}^{-2}$ . The precipitation into basin  $n$  is also split into a constant value and an anomaly:  $P_n(t) = P_{n0} + P_n^*(t)$ . The assumption is now that the zonally averaged anomaly  $\bar{P}^*$  will be equally distributed into the different basins. This means  $P_n^* = 2\pi\bar{P}^* / \sum \Delta\Lambda_n$ .

The determination of the eddy-diffusion coefficients  $K_T$  and  $K_q$  involves the fluxes of heat and freshwater at the ocean's surface at the time of coupling. The calculation of the eddy-diffusion coefficient for latent heat is analogous to the one for sensible heat described by

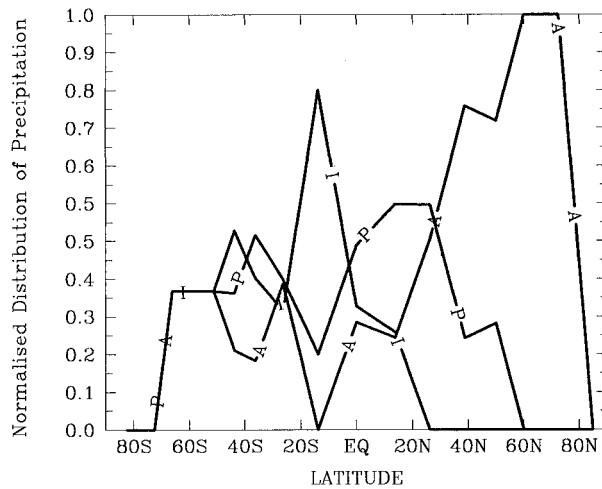


FIG. 2. Latitudinal distribution of the normalized zonal distribution of precipitation into the different basins. A, P, and I denote the Atlantic, Pacific, and Indian Oceans, respectively.

Stocker et al. (1992) and will thus be only briefly discussed here.

The steady-state freshwater flux or, equivalently, the virtual salt flux at the ocean surface,  $Q_s^*$ , is approximately related to  $E - P$  by the following equation:

$$E_n - P_n = -\frac{L\rho_*}{S_*}Q_s^*, \quad (10)$$

where  $S_*$  and  $\rho_*$  are reference salinity and density (Table 1). The eddy diffusion coefficients for water vapor can now be diagnosed by integrating Eq. (9). We obtain

$$K_q(\varphi) = -\frac{a^2}{r \cos \varphi} \left( \frac{\partial q_s}{\partial T} \frac{\partial T}{\partial \varphi} \right)^{-1} \int_{-90^\circ}^{\varphi} (E - P) \cos \varphi \, d\varphi. \quad (11)$$

The right-hand side is determined by the steady-state surface freshwater flux of the ocean model and by the surface air temperature data over the sea from Oort (1983). This method of objective determination of the parameters has the advantage that the model does not drift into a different state after coupling, because it provides the ocean model with the same heat and freshwater fluxes as during spinup. The change of the equilibrium steady state after coupling is very small (e.g., global mean air temperature rises by  $0.02^\circ\text{C}$  and the maximum local SST difference is lower than  $0.1^\circ\text{C}$ ). The use of flux corrections is therefore unnecessary.

The eddy diffusion coefficients determined according to Eq. (11) are shown in Fig. 3. Also plotted are the coefficients for the transport of sensible heat  $K_T$ . While both have the same order of magnitude, negative values may be diagnosed for  $K_q$  as found in earlier studies (Ghil 1976; Harvey 1988; Chen et al. 1995). This indicates the inappropriateness of the diffusive parameterization [Eq. (4)] in these regions. One could argue that the mean meridional circulation, for example, the equatorial Had-

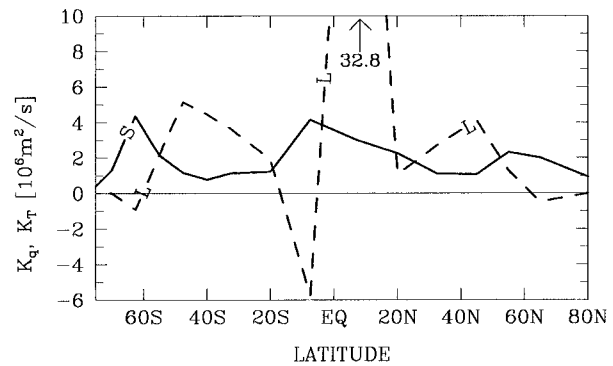


FIG. 3. Atmospheric meridional eddy diffusivity for sensible heat (S),  $K_T$ , and water vapor (L),  $K_q$ .

ley cell, transports water vapor against the gradient, but nevertheless, we do not think that negative diffusion coefficients are a sensible choice. A representation of the mean circulation, especially near the equator, where the transport is not primarily due to transient eddies is attempted in section 3d, where the influence of the local occurrence of negative eddy diffusivities is discussed.

### 3. Global warming simulations

Greenhouse gases ( $\text{H}_2\text{O}$ ,  $\text{CO}_2$ ,  $\text{CH}_4$ , and others) have the property to absorb infrared radiation and to reemit it isotropically. For light with shorter wavelengths, like ultraviolet or visible radiation, they are transparent. The earth's surface and the relatively warm near-surface air masses emit longwave radiation at their temperature approximately like a graybody. Part of this radiation is absorbed by the greenhouse gases above and reemitted back to the surface, which leads to higher surface temperatures compared to an atmosphere without greenhouse gases. This was already suggested by Fourier (1824), who first mentioned that the atmosphere acts much like the glass of a greenhouse. The net effect at the top of the troposphere can be described as a reduction of outgoing longwave radiation. Increasing the concentration of greenhouse gases in the troposphere will therefore increase the net incoming radiation at the top of the atmosphere. This leads to a warming of the underlying air. First quantitative estimates of the warming due to the anthropogenic  $\text{CO}_2$  emissions were done by Arrhenius (1896), who computed an increase of surface temperature by some  $5^\circ\text{--}6^\circ\text{C}$  for a doubling of atmospheric  $\text{CO}_2$ . A review of the exciting scientific history of  $\text{CO}_2$  can be found in Revelle (1985).

Modern predictions of the global equilibrium surface air temperature rise for a doubling of atmospheric  $\text{CO}_2$  based on current three-dimensional general circulation models lead to a range between  $2.1^\circ$  and  $4.6^\circ\text{C}$  (Houghton et al. 1996). This is due to different representations of land surface, cloud, and sea ice processes as well as the specific oceanic components. In our energy balance model we can select the value of the global mean equi-



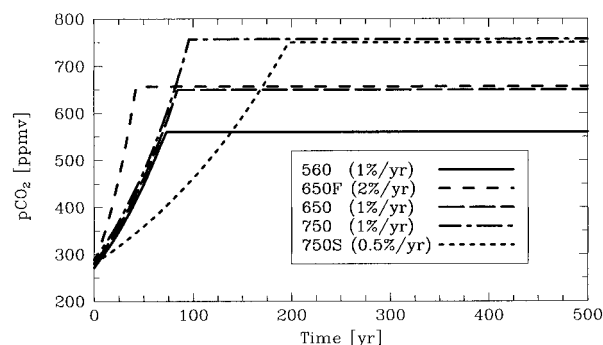


FIG. 4. Prescribed evolution of atmospheric  $\text{CO}_2$  (equivalent greenhouse gases) for the five global warming experiments of (Stocker and Schmittner 1997). The standard rate of  $\text{CO}_2$  increase is  $1\% \text{ yr}^{-1}$  compounded (corresponds approximately to today's growth rate); experiments with a fast rate of  $2\% \text{ yr}^{-1}$  (denoted by F) and a slow rate of  $0.5\%$  (denoted by S) are also given. The maximum  $\text{CO}_2$  values are 560 ppmv (expt 560), 700 ppmv for experiments 700 and 700F, and 750 ppmv for experiments 750 and 750S. Once the maximum value is reached,  $p\text{CO}_2(t)$  is held constant. We chose  $\Delta F_{2\times} = 7.3 \text{ W m}^{-2}$  in all experiments (from Stocker and Schmittner 1997).

librium temperature change due to  $\text{CO}_2$  doubling,  $\Delta T_{2\times}$ , because of the absence of a radiation model. This requires the parameterization of the relationship between  $p\text{CO}_2$  and the perturbation radiative flux  $\Delta F$  at the top of the atmosphere. We thus use a climate sensitivity parameter,  $\Delta F_{2\times}$ , which determines the global equilibrium surface air temperature rise for a doubling of  $p\text{CO}_2$  from the preindustrial level of 280–560 ppmv. The forcing at the top of atmosphere is calculated by the following equation (Shine et al. 1995):

$$\Delta F(t) = \Delta F_{2\times} \ln \left[ \frac{p\text{CO}_2(t)}{280 \text{ ppmv}} \right] / \ln(2), \quad (12)$$

where  $\Delta F(t)$  is the perturbation of the radiative flux in watts per square meter. It is a function of the atmospheric  $\text{CO}_2$ -equivalent greenhouse gas concentration  $p\text{CO}_2$ . For  $p\text{CO}_2$  we assume an exponential growth in time,

$$p\text{CO}_2(t) = (280 \text{ ppmv}) \exp(\gamma t), \quad (13)$$

with different rates of increase  $\gamma$ . Once a preselected maximum concentration is reached,  $p\text{CO}_2$  is kept fixed henceforth.

Figure 4 shows the prescribed atmospheric  $\text{CO}_2$  concentration for five global warming experiments already discussed in Stocker and Schmittner (1997). Here we want to discuss the model results in greater detail. In these experiments we have selected the climate sensitivity  $\Delta F_{2\times}$  such that the global mean surface air temperature difference for a  $\text{CO}_2$  doubling,  $\Delta T_{2\times}$ , agrees with that of Manabe and Stouffer (1993). The global mean equilibrium warming is the global mean surface air temperature difference after 10 000 yr of integration. For  $2 \times \text{CO}_2$  it is  $3.7^\circ\text{C}$  (expt 560) and  $7.3^\circ\text{C}$  for  $4 \times \text{CO}_2$ . This sensitivity is in the intermediate range of that

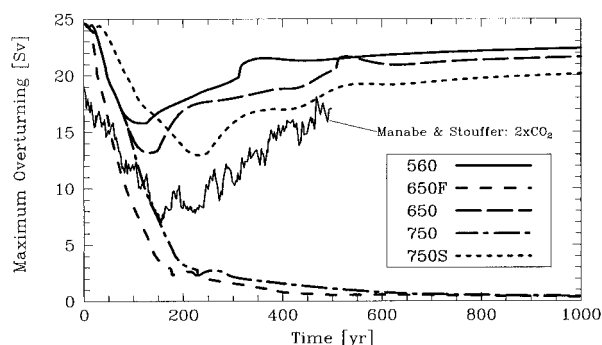


FIG. 5. Evolution of the maximum meridional overturning in the Atlantic Ocean in Sverdrups ( $1 \text{ Sv} = 10^6 \text{ m}^3 \text{ s}^{-1}$ ). The circulation reduces in all cases during the increase of greenhouse gases. Integrations 560, 650, and 750S show a recovery, while the circulation shuts down for the 650F and 750 integrations. For the experiments with the actual rate of  $p\text{CO}_2$  increase (560, 650, 750) the threshold value for a breakdown lies between 650 and 750 ppmv. If the rate of increase is faster ( $2\% \text{ yr}^{-1}$ , expt 650F) the breakdown already occurs below 650 ppmv while for a slower increase (expt. 750S) the threshold value is higher than 750 ppmv. The evolution of the meridional overturning in the Atlantic as calculated in a  $2 \times \text{CO}_2$  experiment with a three-dimensional, coupled atmosphere–ocean general circulation model (Manabe and Stouffer 1994, thin solid line) can be directly compared with our expt. 560. Generally, their model shows a smaller overturning, but the timescales for the reduction and the following recovery are in good agreement with the present results.

reported by Houghton et al. (1996). Note that closure P1 (see section 2) is used in the following unless otherwise stated.

#### a. Linear changes

The global mean air temperature changes at equilibrium are nearly linearly related to the forcing [Eq. (12)]. After 1000 yr they only depend on the final  $\text{CO}_2$  concentration but not on different growth rates. The maximum meridional streamfunction in the Atlantic is shown in Fig. 5. For a doubling of  $\text{CO}_2$  (expt 560) the overturning circulation in the Atlantic reduces by a maximum of about 34% but recovers in the following to a steady-state reduction of about 10%. The thermohaline circulation of this model version exhibits therefore a lower sensitivity than that of Manabe and Stouffer (1994) (maximum reduction: 50%). The timescale of the reduction of the circulation and its subsequent recovery simulated in experiment 560 are in good agreement with those of Manabe and Stouffer (1994). This suggests that the present model captures well the major large-scale processes that are relevant for these experiments.

Two snapshots of the temperature and salinity changes in the Atlantic Ocean during experiment 560 are shown in Fig. 6. At year 100 after the beginning of the warming, around the time of the maximum reduction of the Atlantic overturning, the excess heat has penetrated the upper 1000 m of the ocean with little changes at different latitudes. The salinity, on the other hand, in-

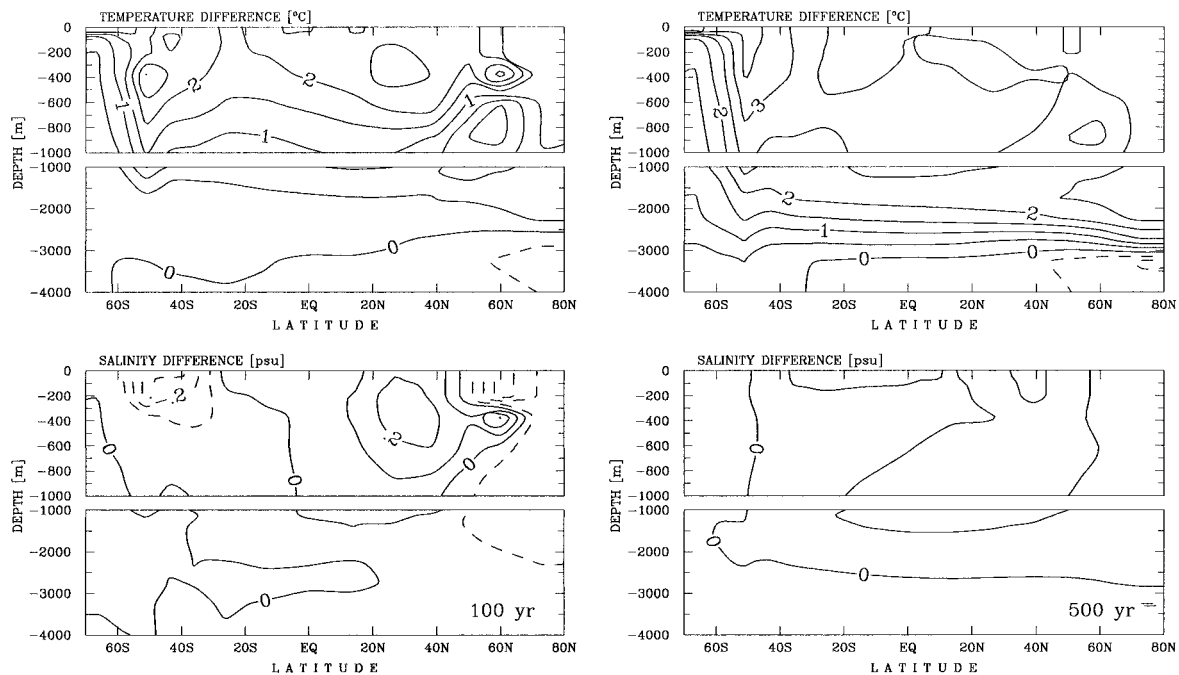


FIG. 6. Latitude–depth distribution of changes of temperature (top, contour interval  $0.5^{\circ}\text{C}$ ) and salinity (bottom, contour interval 0.1) in the Atlantic Ocean of expt. 560. Differences between the initial state and year 100 (left panel) and year 500 (right panel) are shown. Dashed lines indicate negative values of the isolines. The local maxima in both temperature and salinity anomaly distributions after 100 yr at  $60^{\circ}\text{N}$  and 400-m depth are due to reduced convection depth there.

creased mostly at low latitudes, whereas the surface waters are fresher at high latitudes in both hemispheres. These anomalies could develop because the timescale of the forcing was faster than the timescale on which the ocean mixes the additional heat and freshwater to the deep ocean. This leads to a substantially reduced meridional overturning (see Fig. 5). However, at year 70, after which the perturbation fluxes are kept constant, deep water formation in the North Atlantic is still strong enough to efficiently mix the excess freshwater from the surface to the deep ocean. As a consequence the buoyancy anomalies are reduced and the overturning

strengthens again. At year 500 the circulation has recovered to nearly 90% of its initial value. This leads to a warming of the deep ocean, whereas the salinity distribution is close to the initial steady state (Fig. 6).

Air temperature (Fig. 7) has warmed up by about  $3^{\circ}\text{C}$ , nearly independent of latitude, at year 100 of experiment 560. Since surface waters at high latitudes are still convectively mixed with the cold water of the deep ocean, they keep the air temperatures relatively cold. After year 100 high-latitude air temperatures increase more than temperatures at low latitudes. At year 500 the deep ocean has already warmed up, and high-latitude surface waters get warmer (Fig. 6) and can now take up less energy from the atmosphere. This results in a significantly delayed warming of the high latitudes.

Warming of atmospheric temperatures has important consequences for the atmospheric hydrological cycle. Since the ability of the air to hold water vapor is strongly dependent on temperature [Eqs. (6) and (7)], the meridional water vapor flux is increased in a warmer climate. For experiment 560, this is shown in Fig. 8, where the differences of sensible and latent atmospheric meridional heat fluxes between the initial steady state and year 500 are shown. Note that this plot is not shown for year 100 because the differences between years 100 and 500 are very small. With the exception of the southern boundary of the equatorial cell (at  $7.5^{\circ}\text{S}$ ) the sensible heat flux shows small changes. The poleward flux of water vapor or latent heat, on the other hand, has in-

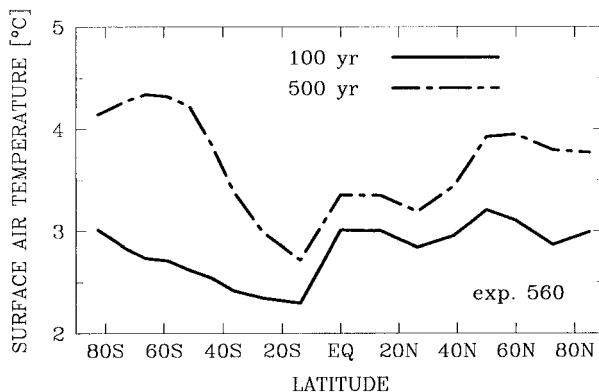


FIG. 7. Difference of the atmospheric air temperatures between the initial steady state and the state at year 100, respectively, year 500 of expt 560.

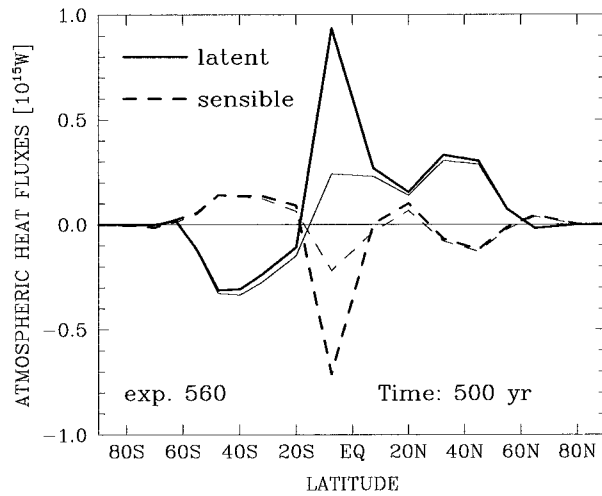


FIG. 8. Difference of the atmospheric heat fluxes (positive northward) between the initial steady state and the year 500 of expt 560 (thick lines). The thin lines are the result of the same run with a model version that avoids negative diffusivities (see below).

creased at every latitude with fairly large changes at  $7.5^\circ\text{S}$ . At this latitude we diagnosed a large negative eddy diffusivity (see Fig. 3), which is responsible for this feature. In section 3d we present a formulation of the hydrological cycle that avoids negative diffusivities and we show that the peaks (in Fig. 8) at the southern boundary of the equatorial cell disappear.

According to Eq. (5) the meridional moisture flux depends on the temperature gradient  $\nabla T$  and on  $\partial q_s/\partial T$ . In order to examine which of these factors is responsible for the increased latent heat flux, we take a look at their relative changes. Let  $\delta_q$ ,  $\delta_T$ , and  $\delta_L$  be the relative changes of  $\partial q_s/\partial T$ ,  $\nabla T$ , and  $L$  respectively:

$$\frac{\partial q_s}{\partial T} = (1 + \delta_q) \frac{\partial q_s}{\partial T}(t_0), \quad \nabla T = (1 + \delta_T) \nabla T(t_0),$$

$$L = (1 + \delta_L) L(t_0), \quad (14)$$

where  $t_0$  denotes the time at the initial steady state. For the year 500 of experiment 560 the relative changes  $\delta_q$ ,  $\delta_T$ , and  $\delta_L$  are shown in Fig. 9. The meridional temperature gradient contributes only little to the changes of latent heat except at the southern boundary of the equatorial cell, where diffusivities are negative. At all other latitudes the dominant term is  $\partial q_s/\partial T$ . The higher values of this term at high latitudes are due to the stronger temperature increase there (Fig. 7) as well as to the fact that the relative change of  $\partial q_s/\partial T$  is temperature dependent. It varies, for example, from about 7.6% at  $-20^\circ\text{C}$  to 5.6% at  $20^\circ\text{C}$  for a temperature change of  $1^\circ\text{C}$ .

The stronger poleward water vapor transport leads to an excess of precipitation over evaporation at middle and high latitudes. Figure 10 shows the differences in evaporation ( $E$ ), precipitation ( $P$ ), and surface freshwater flux ( $E - P$ ) at year 500 as a function of latitude.

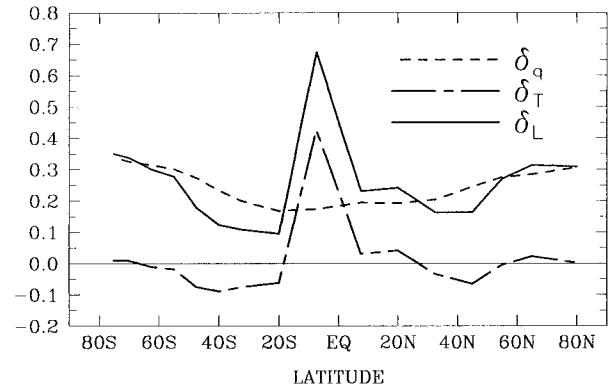


FIG. 9. Relative changes of  $\partial q_s/\partial T$  ( $\delta_q$ ),  $\nabla T$  ( $\delta_T$ ) and the latent heat flux  $L$  ( $\delta_L$ ) as defined in Eq. (14) between the initial steady state and year 500 of expt 560.

Again, for year 100 only small deviations can be seen, and therefore the plot has been omitted. Evaporation has increased at all latitudes with the biggest values at low latitudes and minimum values at high latitudes. Except for the grid point south of the equator, precipitation has increased at every latitude, too. However, we find local maxima at high latitudes that lead to a stronger freshwater input in the oceans there. This picture is qualitatively similar to the findings of Manabe and Stouffer (1994).

#### b. Nonlinear changes

For a rate of  $\text{CO}_2$  increase of  $1\% \text{ yr}^{-1}$  (compounded) the thermohaline circulation breaks down for final  $\text{CO}_2$  concentrations of 750 ppmv or higher (Fig. 5). The circulation settles into a structurally different equilibrium state that is characterized by the complete absence of

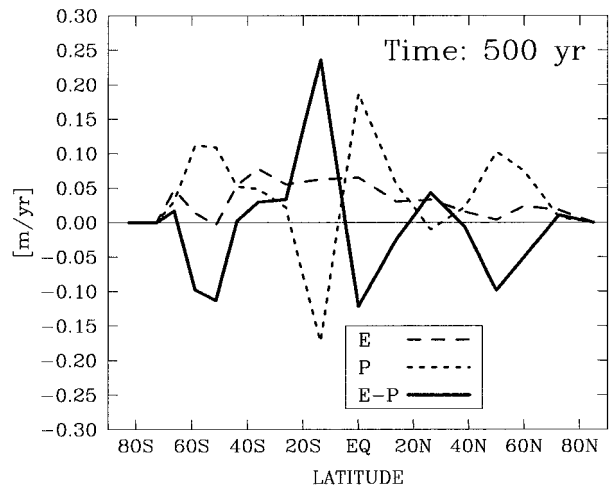


FIG. 10. Latitudinal distribution of the differences in evaporation ( $E$ ), precipitation ( $P$ ), and the freshwater flux from the ocean to the atmosphere ( $E - P$ ) between the initial steady state and year 500 of expt 560.

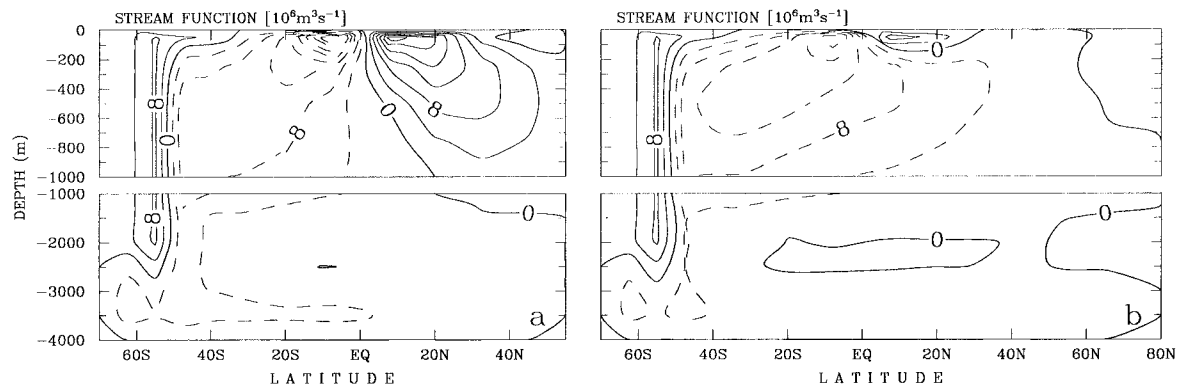


FIG. 11. Modeled meridional overturning streamfunction in the Pacific (a) and the Atlantic (b) for expt 750 at year 1000 after the start of the global warming. Deep water formation in the North Atlantic is collapsed (Fig. 1) while the formation of Antarctic Bottom Water is only slightly reduced.

deep water formation in the North Atlantic (see Fig. 11); no further changes were observed in 10 000-yr integrations. The threshold value of the maximum  $p\text{CO}_2$ , beyond which nonlinear changes occur, depends on the climate sensitivity parameter  $\Delta F_{2\times}$  and on other model parameters.

An important finding of these model experiments is that the threshold value also depends on the rate of  $\text{CO}_2$  increase (Stocker and Schmittner 1997). For a slower increase ( $0.5\% \text{ yr}^{-1}$ , expt. 750S) the circulation recovers even for final  $\text{CO}_2$  concentrations of more than 750 ppmv. A faster increase ( $2\% \text{ yr}^{-1}$ , expt. 650F), on the other hand, will further destabilize the ocean-atmosphere system, and the thermohaline circulation of the North Atlantic already breaks down for values below 650 ppmv (Fig. 5).

The shutdown of the Atlantic thermohaline circulation has a major impact on the oceanic temperature distribution. In Fig. 12 the temperature change between the initial steady state and that after 1000 yr of integration is shown for experiment 750. Despite the global mean warming of more than  $5^\circ\text{C}$  northern North Atlantic waters between  $60^\circ$  and  $80^\circ\text{N}$  in surface and subsurface

regions are colder compared to a climate with an active thermohaline circulation. This is due to the absence of poleward advection of warm tropical and subtropical water masses and to the asymmetric warming of the hemispheric air masses (see below). Southern Hemisphere waters between the surface and 1000-m depth, on the other hand, show the strongest warming. The maximum occurs at about  $40^\circ\text{S}$  in the subsurface waters at 400-m depth in the Atlantic Ocean. The reason for this asymmetric temperature signal is that the meridional overturning no longer draws heat from the Southern Hemisphere (Crowley 1992).

The latitudinal distribution of the surface air temperature differences between the start and the end of experiments 560, 750, and 750S is shown in Fig. 13. For the cases with an active Atlantic thermohaline circulation (expts 560, 750S) the warming is largest at high and middle latitudes. This is also consistent with three-dimensional model results (Cubasch et al. 1992). For the case in which the Atlantic thermohaline circulation shut down the warming is enhanced in the Southern Hemisphere. This is due to the stopped Atlantic heat transport from the Southern to the Northern Hemisphere.

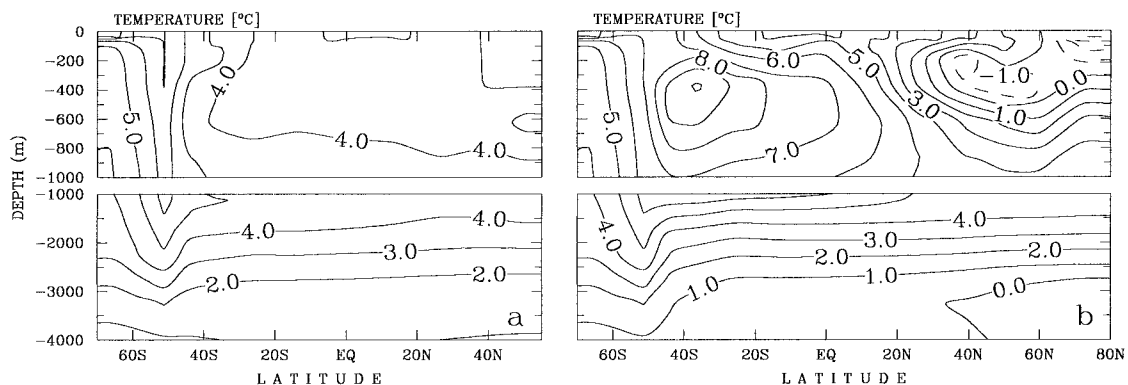


FIG. 12. Latitude-depth distribution of the temperature difference between the start and the end (1000 yr) of expt 750 in the Pacific (a) and Atlantic (b) Oceans.



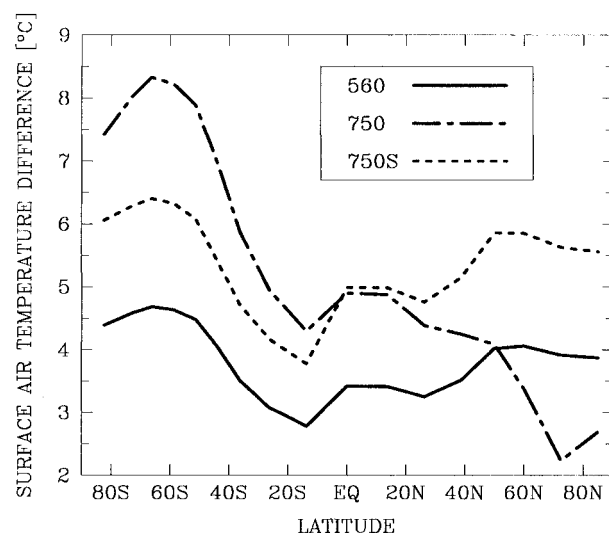


FIG. 13. Latitudinal profiles of the near-surface air temperature rise for experiments 560, 750, and 750S. In the cases, where the Atlantic thermohaline circulation is still operating (expts 560 and 750S), the maximum warming occurs at mid- and high latitudes of both hemispheres. The warming is asymmetric between the hemispheres if the circulation breaks down (expt 750). The Atlantic Ocean transports about 1 PW ( $=10^{15}$  W) of heat from the Southern Hemisphere to the Northern Hemisphere if the thermohaline circulation is on. In the absence of this circulation, excess heat remains in the Southern Hemisphere, resulting in a stronger warming there.

sphere. The differences in global meridional heat fluxes between the states with the circulation “on” and “off” are plotted in Fig. 14. The switch off of the North Atlantic heat pump is only partly compensated by additional northward atmospheric heat transport.

### c. The influence of the hydrological cycle

Manabe and Stouffer (1994) already found that the main reason for the breakdown of the thermohaline circulation in their global warming experiments was the capping of high-latitude oceans by relatively fresh, low-density water. The enhanced water vapor transport in the warmer atmosphere leads to an excess of precipitation over evaporation in middle and high latitudes. In our model this is represented through the strong dependency of  $\partial q_s / \partial T$  on temperature [Eq. (7)]. The increased atmospheric water vapor (or latent heat) transport of integration 750 is qualitatively similar to the changes observed in experiment 560 (Fig. 8) but higher in magnitude. At nearly all latitudes the equator-to-pole transport of water vapor has increased by about 30%. The differences in evaporation  $E$ , in precipitation  $P$ , and in  $E - P$  between the initial state and year 1000 of experiment 750 are again similar to those of experiment 560 (see Fig. 10) with higher amplitudes. Evaporation has increased everywhere except over the northern North Atlantic, which is due to the decreased difference between sea surface temperature and air temperature there. Precipitation, however, increased mainly pole-

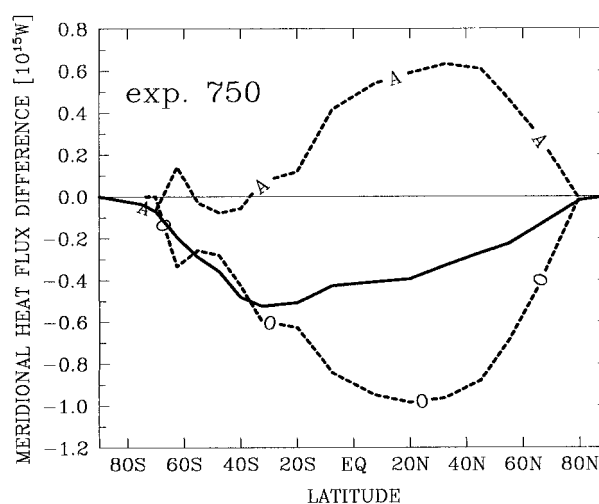


FIG. 14. Differences of meridional (northward) heat fluxes between the start and the end of expt 750. The atmospheric heat flux (A) consists of the sensible and the latent heat fluxes. The difference in the oceanic heat flux (O) is mainly due to the breakdown of the Atlantic thermohaline circulation. It is partly compensated by the atmosphere but the residual additional southward flux (solid) has a maximum of about 0.5 PW.

ward of  $30^\circ$  in both hemispheres, which results in an additional freshwater flux into the mid- and high-latitude oceans.

Time series of precipitation, evaporation, sea surface salinity (SSS), sea surface temperature (SST), and  $\sigma_t$  (see Gill 1982, 601, for definition) in the Atlantic at  $60^\circ\text{N}$  for experiment 750 are shown in Fig. 15. During the first 100 yr precipitation and sea surface temperature are increasing nearly linearly in time, except for some changes of convection. The first change in convection at  $60^\circ\text{N}$  occurs at year 46, when convection depth shallows from 500 to 250 m. This leads to a sudden decrease in SST, precipitation, and evaporation. The next more dramatic event happens during years 86 and 89, when convection reaches only 150 m (year 86) and finally stops (year 89). Again, precipitation, evaporation, and SST decrease, but SSS and sea surface density ( $\sigma_t$ ) also decrease substantially due to the shutdown of convection. The freshwater flux into the ocean ( $P - E$ ) increases during warming until year 100 and remains approximately constant afterward. Sea surface salinity is decreased only slightly during the first 90 yr, mainly due to increased  $P - E$ . Once a certain threshold value of  $\sigma_t$  is reached, convection stops, leading to an irreversible reduction of density and salinity at the sea surface.

We now examine changes in the density structure of the Atlantic Ocean. To discriminate between the temperature-induced and the salinity-induced density changes we follow Manabe and Stouffer (1994) and calculate the differences in  $\sigma_t$  due to temperature changes only,

$$\Delta_T \sigma_t = \sigma_t[T(t_1), S(t_0)] - \sigma_t[T(t_0), S(t_0)], \quad (15)$$

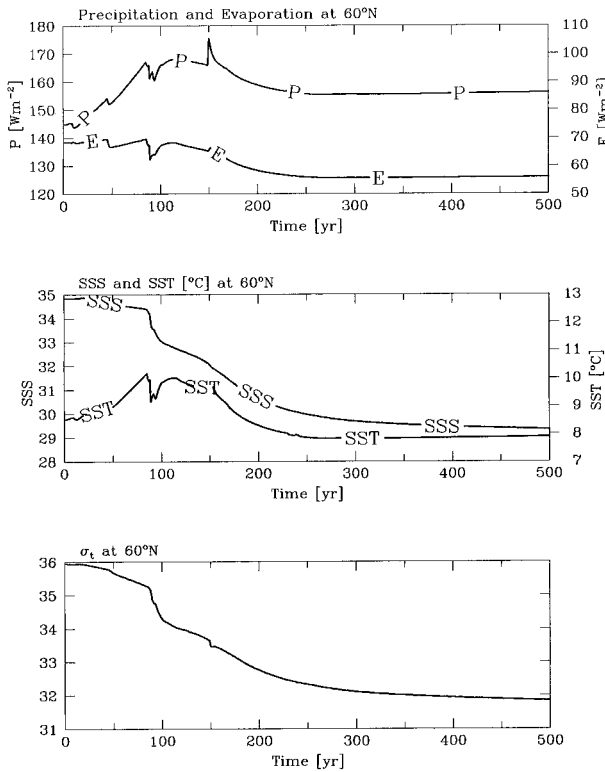


FIG. 15. Evolution (top) of precipitation ( $P$ , left axis) and evaporation ( $E$ , right axis), (middle) of sea surface salinity (SSS, left axis) and sea surface temperature (SST, right axis), and (bottom) of sea surface  $\sigma_t$  (density) at 60°N in the Atlantic (all from expt 750). Sudden changes of the various variables are due to changed convection depths. The peak in precipitation at year 150 is due to changes in North Pacific convection.

and due to salinity changes only,

$$\Delta_s \sigma_t = \sigma_t[T(t_0), S(t_1)] - \sigma_t[T(t_0), S(t_0)], \quad (16)$$

where temperature and salinity fields were taken at  $t_0 = 0$  yr and  $t_1 = 1000$  yr of experiment 750. Figure 16 shows that the density change due to salinity is responsible for the strong minimum in  $\Delta \sigma_t$  in the North Atlantic while the warming of the ocean from above tends to increase the stability of the water column in the rest of the Atlantic Ocean. An analysis of the  $\Delta_T \sigma_t$  and  $\Delta_s \sigma_t$  fields of experiment 750 indicates that during the first 70 yr both terms contribute to lower densities in the northern North Atlantic. The influence of temperature is dominant during the first 40–50 yr and salinity effects increase in importance after 70 yr. Different feedback mechanisms between the advection of tropical and subtropical warm and saline water masses and the deep water formation in the North Atlantic are the reason for this. The advection of warm (light) water to the north is a negative feedback on the deep water formation, while the advection of saline (dense) water has a positive feedback effect on the thermohaline circulation. In turn, a weakened circulation tends to decrease North Atlantic salinities and temperatures.

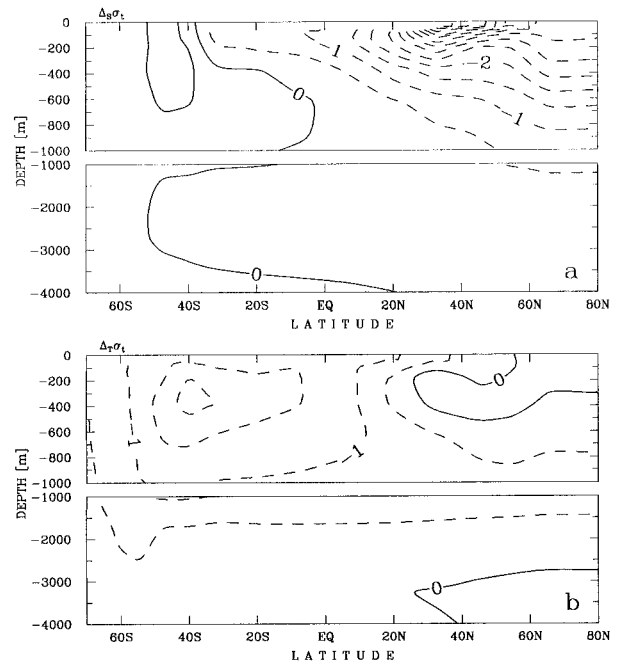


FIG. 16. Latitude–depth distribution  $\Delta_s \sigma_t$  (a) and  $\Delta_T \sigma_t$  (b) in the Atlantic Ocean (expt 750)

Although it seems to be a combined effect of warming and freshening of the North Atlantic surface waters, at least at the beginning of the experiments, an active hydrological cycle is crucial for the existence of a realistic threshold value for  $p\text{CO}_2$ . An additional model run with an extremely strong and quick forcing in which  $p\text{CO}_2$  was increased eightfold in 52 yr ( $\gamma = 4\% \text{ yr}^{-1}$ ) showed no breakdown of the circulation if the hydrological cycle ( $E - P$ ) was kept fixed at present day values.

The increased equator-to-pole latent heat transport in a greenhouse climate is also the reason for the increased warming of high-latitude air masses. This is shown in Fig. 17, where the latitudinal profile of the surface air temperature rise of integration 750S is compared with

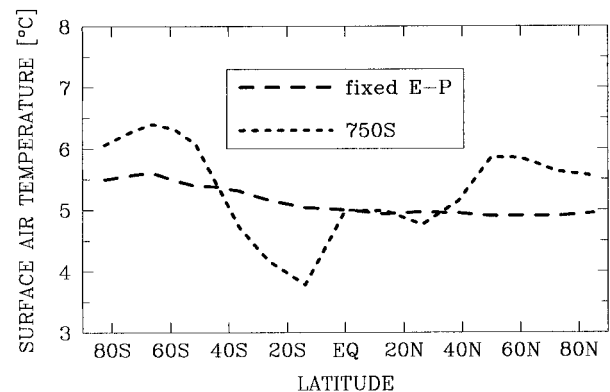


FIG. 17. Latitudinal distribution of surface air temperature rise of integrations 750S and the same integration with a fixed hydrological cycle.

the same integration using a fixed hydrological cycle. The warming is nearly uniform at all latitudes if  $E - P$  is held constant.

#### d. The influence of negative diffusivities

In order to examine the influence of the negative eddy diffusion coefficients (Fig. 3) we developed a simple alternative formulation of the hydrological cycle, in which the diffusivities are kept positive everywhere. The occurrence of negative diffusivities shows that the assumption of a purely diffusive meridional transport fails at those latitudes. The mean meridional circulation (e.g., the Hadley cell in the equatorial region) does not necessarily transport properties down gradient. In our simple energy balance model of the atmosphere we add a latitude-dependent meridional wind velocity,  $v$ , which represents the mean circulation. This leads to an additional meridional advective water vapor flux,  $vq$ , which is independent of the moisture gradient  $\partial q/\partial y$ . Instead of Eq. (4) we write for the total meridional flux of specific humidity

$$\mathbf{L} = vq - K_q \frac{\partial q}{\partial y}. \quad (17)$$

Since we do not have a dynamic model, we have to make an assumption concerning the velocity  $v$ . A crude assumption is to fix  $v$  implying that the mean circulation does not change, while the flux  $vq$  is variable since  $q = r \cdot q_s(T)$ , and  $T$  may change in time.

Equation (17) is used only at those latitudes where the diffusive parameterization is obviously inappropriate. This is done by limiting the diffusivities to  $10^6 \text{ m}^2 \text{ s}^{-1} \leq K_q \leq 10^7 \text{ m}^2 \text{ s}^{-1}$ . Where this limitation is violated at the time of coupling, we set the diffusion coefficient to its minimal value  $K_q = 10^6 \text{ m}^2 \text{ s}^{-1}$  and diagnose the advection velocity according to

$$v = \frac{a}{q \cos \varphi} \int_{-90^\circ}^{\varphi} (E - P) \cos \varphi \, d\varphi + \frac{K_q}{qa} \frac{\partial q}{\partial \varphi}. \quad (18)$$

This procedure is consistent with diagnosing  $K_q$  and guarantees a stable climate after coupling. At all other latitudes we set  $v = 0$ . Figure 18 shows the velocities diagnosed in the above-described manner. Only at the boundaries of the equatorial grid cell, at  $62.5^\circ\text{S}$ , and at  $65^\circ\text{N}$  is an advection velocity diagnosed. These can be interpreted as the effects of the Hadley cell and the polar vortices, respectively. The order of magnitude is consistent with data from annual mean near-surface meridional wind velocities (Peixoto and Oort 1992). Also shown in Fig. 18 is the latent heat transport associated with these velocities and the total meridional latent heat flux. Although the velocities diagnosed at high latitudes are of the same order of magnitude as those at low latitudes, the advective latent heat flux is only important near the equator because of very small  $q$  at high latitudes.

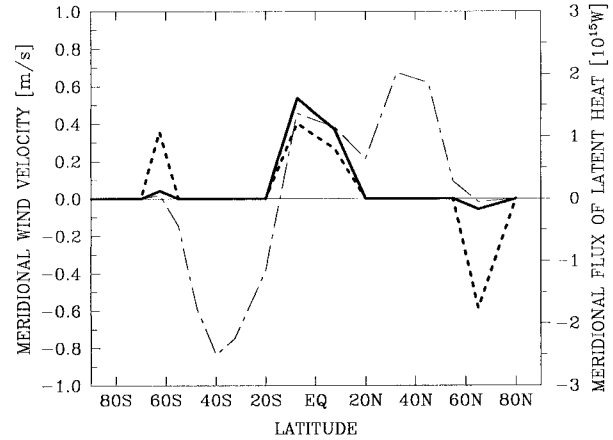


FIG. 18. Profiles of the mean meridional wind velocity (dotted) diagnosed according to Eq. (18), the meridional advective flux of latent heat (thick solid), and the total meridional flux of latent heat (thin dashed-dotted) at the initial steady state.

Some of the global warming experiments described in the previous sections were redone with this formulation of the hydrological cycle. Differences to the model results already presented occurred mainly near the equator. The thin lines in Fig. 8 show the differences in the heat fluxes between the initial state and year 500 of a  $\text{CO}_2$  doubling experiment based on the formulation of the hydrological cycle including advective transport. Compared with the version including negative diffusivities (thick lines), it is obvious that the peaks south of the equator have disappeared, but at all other latitudes the results are nearly identical.

This is also true for the calculated precipitation and for the surface freshwater flux  $E - P$ . The peaks in  $P$  and  $E - P$  in Fig. 10 at the equator and south of it have disappeared with the formulation excluding negative diffusivities, while at other latitudes only minor changes occur.

The sensitivity of the thermohaline circulation to the global warming is slightly reduced (more details in section 4), but all general features from the model version with negative diffusivities, as described above, are not altered.

#### e. Ice-albedo feedback

In a warmer climate snow and sea ice cover in high latitudes may be significantly reduced, which will modify the radiation balance. The ice-albedo feedback is one of the primary mechanisms for long-term climate variability (Crowley and North 1991). To examine the effect of a temperature-dependent albedo on the model results we included the following simple parameterization:

$$\alpha = \alpha_0(\varphi) + \beta \tanh\left(\frac{273 \text{ K} - T}{10 \text{ K}}\right). \quad (19)$$

This is a smoothed version of the ramp-type parameterization proposed by Sellers (1969), Ghil (1985), and others, where  $\beta$  is a constant. Values of the albedo were restricted to the range 0.05–0.95. The albedo is assumed to vary mainly in regions with temperatures between  $-10^\circ$  and  $10^\circ\text{C}$ , where snow and sea ice cover are neither perennial nor absent.

The latitude-dependent constant  $\alpha_0$  will be determined at the time of coupling of the atmosphere and ocean models as follows. We diagnose the planetary albedo  $\alpha^*(\varphi)$  from the annually averaged solar shortwave radiation at the top of atmosphere,  $Q$ , and the net incoming shortwave radiation  $F^{sw}$ , determined from the data of Stephens et al. (1981) according to

$$\alpha^*(\varphi) = 1 - \frac{F^{sw}}{Q}. \quad (20)$$

The latitude-dependent constant  $\alpha_0$  is then calculated by inverting Eq. (19):

$$\alpha_0(\varphi) = \alpha^*(\varphi) - \beta \tanh\left(\frac{273 \text{ K} - T}{10 \text{ K}}\right). \quad (21)$$

It is well known that the inclusion of a temperature-dependent albedo in a climate model can lead to additional equilibria, like, for example, a totally ice-covered earth (Sellers 1969). Indeed, this has also been found in the present study.

To test the sensitivity of the model response to different values of the slope  $\beta$  we performed four experiments. Additionally, we compare the meridional distribution of the near-surface air temperature change with results from a three-dimensional model. Cubasch et al. (1995) performed a global warming experiment in which they increased  $p\text{CO}_2$  at a rate of  $0.12\% \text{ yr}^{-1}$  for 100 yr (from 1985 to 2085), including the effect of early industrialization (observed  $\text{CO}_2$  concentration from 1935 to 1985). After 100 yr the mean near-surface temperature difference is  $3.3^\circ\text{C}$  for their cold-start corrected integration. For each integration of our model with a different slope  $\beta$  we choose the climate sensitivity parameter  $\Delta F_{2\times}$  such that the global mean warming at year 100 was approximately  $3.3^\circ\text{C}$ . The meridional distribution of the temperature rise after 100 yr is shown in Fig. 19. Note that closure P1 for the zonal distribution of precipitation and the inclusion of an advective part of the water vapor transport (described in the preceding section) was used here. The result from Cubasch et al. (1995) shows a warming of  $2.5^\circ\text{--}3^\circ\text{C}$  at low latitudes and midlatitudes (between  $60^\circ\text{S}$  and  $60^\circ\text{N}$ ) and maxima of more than  $6^\circ\text{C}$  at  $70^\circ\text{S}$  and more than  $5^\circ\text{C}$  at  $75^\circ\text{N}$ . Comparison with Fig. 19 shows qualitative agreement with their three-dimensional model response. Increasing slope  $\beta$  increases the warming at high latitudes and decreases the warming at low latitudes. Best agreement of the absolute difference between the minima and maxima of the latitudinal warming with Cubasch et al. (1995) is found for the highest value of  $\beta = 0.17$ , al-

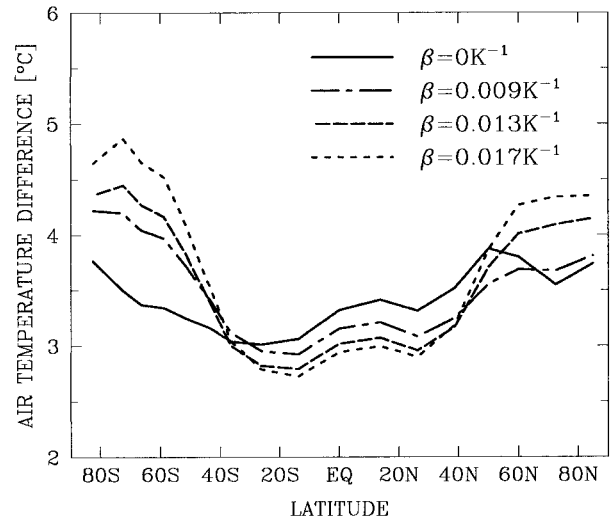


FIG. 19. Meridional distribution of temperature rise for different values  $\beta$  in the ice-albedo parameterization. Here  $\Delta F_{2\times}$  was chosen such that the global mean warming is  $3.3^\circ\text{C}$  in all experiments. Differences were calculated between the initial states and that after 100 yr for comparison with Cubasch et al. (1995).

though our maxima are still lower than theirs. Another difference is that the high-latitude maxima are farther poleward in Cubasch et al. (1995). Such a result could be achieved by shifting the  $\tanh$  (Eq. 19) farther to lower temperatures. On the other hand, we do not want to tune the model parameters in a way to get closer to certain 3D models, because this would clearly go beyond the present simplified climate model. Moreover, three-dimensional models themselves show big differences in the latitudinal distribution of the warming. Manabe and Stouffer (1994), for example, obtain very strong maxima at the North Pole, but at southern high latitudes they predict the weakest warming. Gregory and Mitchell (1997) mention that both their flux-adjusted and their non-flux-adjusted 3D model versions show maximum warming at the poles, but a minimum at about  $55^\circ\text{S}$  and a strong asymmetry between the hemispheres. Warming is much bigger at the North Pole than in Antarctica. Syktus et al. (1997) show that the signal-to-noise ratio in an ensemble of global warming experiments from two different general circulation models is larger over low latitudes and lowest over high latitudes. This could be partly due to the uncertainties in the parameterizations of clouds and sea ice properties, resulting in different relations between temperature and planetary albedo.

Another interesting result is the reduction of the meridional overturning in the North Atlantic reported by Cubasch et al. (1995). It diminished by more than 30% by year 100. In our model run with the same mean warming and no ice-albedo feedback the thermohaline circulation is also reduced by 30% at year 100. In the experiments with inclusion of ice-albedo feedback the circulation is weaker. For  $\beta = 0.09$  it is lower than 40%



TABLE 2. Model versions used in the sensitivity studies. Here  $\alpha(T)$  denotes the inclusion of a temperature-dependent albedo, P1 and P2 indicate the different closures for the zonal distribution of precipitation, and  $\lambda$  is the equilibrium climate sensitivity defined as  $\Delta T = \lambda \Delta F + T_0$ . Negative diffusivities occurred in the versions P1A0, P1A1, P2A0, and P2A1. Experiments in which advective moisture transport is included are denoted by the suffix “ad.”

Version	Closure	$\alpha(T)$	$\lambda$ [K (W m <sup>-2</sup> ) <sup>-1</sup> ]	$T_0$ (°C)	$r$
P1A0	P1	no	0.503	-0.015	0.9999752
P1A1	P1	yes	0.619	0.545	0.9989745
P2A0	P2	no	0.500	0.009	0.9999975
P2A1	P2	yes	0.619	0.449	0.9989169
P1A0ad	P1	no	0.500	0.005	0.9999984
P1A1ad	P1	yes	0.607	0.535	0.9985584
P2A0ad	P2	no	0.500	-0.002	0.9999998
P2A1ad	P2	yes	0.582	0.743	0.9987191

of its initial value and for  $\beta = 0.17$  it is reduced by more than 50%. This indicates that the thermohaline circulation in our model is a little more sensitive than that of Cubasch et al. (1995).

#### 4. Results from sensitivity studies

The following sensitivity studies were done for eight different model versions summarized in Table 2. Model version P1A0, for example, used closure P1 (see section 2) for the zonal distribution of precipitation and did not include a temperature-dependent albedo. Note also that the model versions with an advective part of the humidity transport are denoted by the suffix “ad” and for the model versions including ice-albedo feedback the slope  $\beta = 0.09$  was taken.

Current three-dimensional coupled atmosphere–ocean climate models show a considerable range of the predicted equilibrium near-surface air temperature rise for a doubling of atmospheric CO<sub>2</sub>, and  $\Delta T_{2\times}$ , which lies between 2.1° and 4.6°C (Houghton et al. 1996). The

goal of this sensitivity study is therefore to examine possible values of threshold CO<sub>2</sub> concentrations for this range of equilibrium temperature changes. In addition, we investigate the dependency of the breakdown of the Atlantic thermohaline circulation on the rate of change of the forcing at the top of the atmosphere,  $\partial\Delta F/\partial t$ . This was done by taking a fixed value of  $\partial\Delta F/\partial t$ , which is a constant during the time of CO<sub>2</sub> increase according to Eqs. (12) and (13),

$$\frac{\partial\Delta F}{\partial t} = \frac{\Delta F_{2\times}}{\ln 2} \gamma \quad (22)$$

and performing model experiments with different maximum values of the forcing  $\Delta F_{\max}$ . Once  $\Delta F_{\max}$  was reached  $\Delta F$  was held constant. The critical value  $\Delta F_c$  at which the circulation broke down was taken as in between the highest value of  $\Delta F_{\max}$  at which the circulation recovered and the lowest value of  $\Delta F_{\max}$  at which the circulation broke down. This procedure was performed for different values of  $\partial\Delta F/\partial t$ .

Figure 20 shows the critical forcing  $\Delta F_c$  as a function of  $\partial\Delta F/\partial t$  for the model versions of Table 2. The error bar delimits the model runs with the stable and unstable circulation, respectively. Model version P1A1 shows the lowest critical values and thus has the highest sensitivity. Closure P1 leads to higher precipitation into the Atlantic Ocean, compared with closure P2 and thus shows a higher sensitivity, especially for slow rates of change of the forcing. Generally, the versions avoiding negative diffusivities (right panel) show higher values of the critical forcing, which is due to a decreased northward water vapor transport, especially near the equator (Fig. 8).

The inclusion of the positive ice-albedo feedback (A1) generally increases the model sensitivity. This is due to the stronger warming at high latitudes, which leads to further thermal stabilization of the water column. Additionally, freshwater input into high-latitude

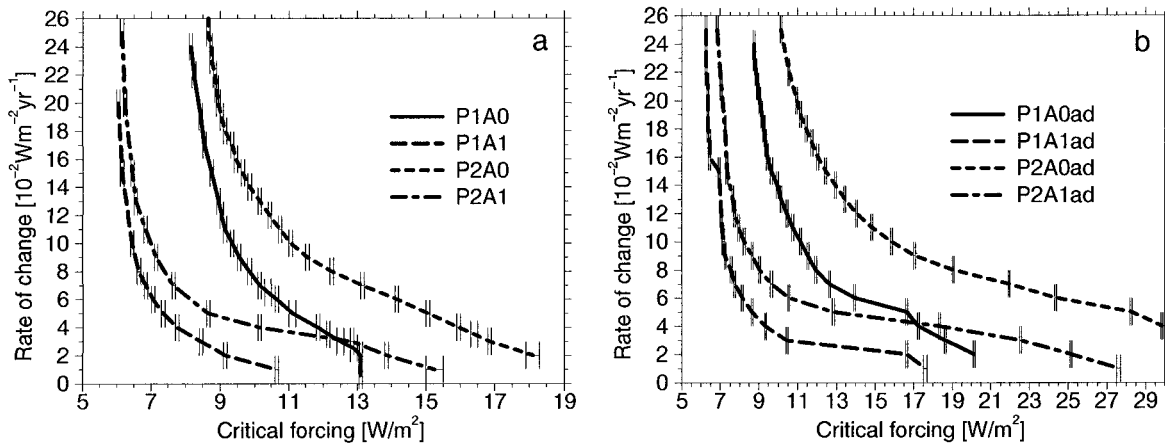


FIG. 20. Critical forcing at the tropopause,  $\Delta F_c$ , at which the thermohaline circulation breaks down as a function of rate of change of the forcing  $\partial\Delta F/\partial t$  for four different model versions (see Table 2). (a) Versions with negative diffusivities. (b) Versions with the inclusion of an advective part of the water vapor transport.



oceans is increased contributing further to the higher sensitivity. Another interesting result is that the influence of the zonal distribution of precipitation (P1 vs P2) on the model response is less when albedo is temperature dependent. The reason for this might be that the ice-albedo feedback, which is a strong positive feedback, dominates second-order effects like the zonal distribution of precipitation.

All model versions exhibit higher critical values for the breakdown of the circulation if the rate of increase is slower. Closure P2 generally leads to a stronger rate sensitivity than closure P1. The timescales for the fast rates of increase of the forcing that lie between about 30 and 50 yr would correspond to the timescales of the convective instability mechanism described by Rahmstorf et al. (1996). For low values of  $\partial\Delta F/\partial t$  the timescales are about 200–500 yr, which corresponds to the advective slowdown timescales already described by Bryan (1986). But it is also clear from Fig. 20 that both processes interact for intermediate rates of change and that the timescales are continuously increasing with decreasing rates of change.

Now we briefly address the stability of the new equilibrium state after the breakdown of the Atlantic thermohaline circulation. Generally, the new equilibrium was stable in 10 000-yr integrations. Exceptions only occurred for model versions P2 for high values of the forcing. For model version P2A0 (P2A0ad) the circulation recovers after it has been “down” for a long time ( $>1000$  yr) for maximum perturbation fluxes of over  $30 \text{ W m}^{-2}$  ( $18 \text{ W m}^{-2}$ ) for slow rates of change ( $3 - 5 \times 10^{-2} \text{ W m}^{-2} \text{ yr}^{-1}$ ). These fluxes lead to global warming of about  $15^\circ\text{C}$ . The reinitiation of the Atlantic overturning seems to be caused by a weakening of the Antarctic bottom water (AABW) production. Antarctic bottom water is the densest water and fills the entire deep ocean thereby stabilizing the water column. If the stabilizing effect of the AABW is weakened it seems to be possible that the Atlantic is destabilized by downward diffusion of heat (Wright and Stocker 1991). The zonal distribution of excess freshwater is important here since a destabilization was only observed for parameterization P2.

From Fig. 20 we now calculate the threshold  $\text{CO}_2$  concentrations as a function of the rate of  $\text{CO}_2$  increase and the equilibrium temperature rise as follows. The critical forcing  $\Delta F_c$  is related to the threshold  $\text{CO}_2$  concentration  $(p\text{CO}_2)_c$  according to

$$\Delta F_c = \frac{\Delta F_{2\times}}{\ln 2} \ln \left[ \frac{(p\text{CO}_2)_c}{280 \text{ ppmv}} \right], \quad (23)$$

which follows from Eq. (12). Solving for  $(p\text{CO}_2)_c$  leads to

$$(p\text{CO}_2)_c = 280 \text{ ppmv} \exp \left( \ln 2 \frac{\Delta F_c}{\Delta F_{2\times}} \right). \quad (24)$$

We took a range of values for  $\gamma$  and  $\Delta F_{2\times}$  and cal-

culated  $\partial\Delta F/\partial t$  according to Eq. (22). For a given  $\partial\Delta F/\partial t$  we determined  $\Delta F_c$  from Fig. 20 and used Eq. (24) to get the corresponding threshold  $\text{CO}_2$  concentration. Finally, the equilibrium climate sensitivity  $\lambda = \Delta T/\Delta F$  of the actual model version was determined by 10 000-yr integrations with different values for  $\Delta F$  (Table 2). A linear regression lead to the climate sensitivities given in Table 2, where the corresponding correlation coefficients  $r$  are also given. For the model versions with ice-albedo feedback a nonnegligible intercept was found. This is due to a nonlinear relation between  $\Delta T$  and  $\Delta F$  for small values of the forcing ( $\Delta F < 2 \text{ W m}^{-2}$ ). For these model versions the equilibrium temperature rise was therefore calculated using  $\Delta T = \lambda\Delta F + T_0$ . The climate sensitivity and the intercept were used to calculate the equilibrium temperature rise for a  $\text{CO}_2$  doubling following  $\Delta T_{2\times} = \lambda\Delta F_{2\times} + T_0$ .

In Fig. 21 isolines of the  $p\text{CO}_2$  threshold value for the breakdown of the thermohaline circulation are shown as a function of  $\Delta T_{2\times}$  and the rate of  $\text{CO}_2$  increase  $\gamma$ . The left panel was produced with the standard model version P1A0. The threshold values decrease with increasing climate sensitivity ( $\Delta T_{2\times}$ ). If the future  $\text{CO}_2$  increase is slower, the maximum  $\text{CO}_2$  concentration in the atmosphere, for which the thermohaline circulation does not permanently shut down, will be higher. The absolute values as well as the shape of the isolines are dependent on the model version. Generally they are higher for the formulation of the hydrological cycle that avoids negative diffusivities. Version P1A0ad, for example, shows 15%–30% higher values and slightly smaller slopes of the isolines.

The zonal distribution of precipitation also has a considerable influence on the results. Threshold  $\text{CO}_2$  concentrations are higher for the equally distributed precipitation anomaly closure (P2). Inclusion of a temperature-dependent albedo has a smaller effect on the values of the threshold concentrations. As an example for very high values, we show the results of model version P2A0ad in the right panel. The  $\text{CO}_2$  threshold concentrations are much larger compared with model version P1A0 as expected from Fig. 20. For values of  $\gamma = 1\% \text{ yr}^{-1}$  and  $\Delta T_{2\times} = 3.7^\circ\text{C}$  (cf. with Fig. 21) we get a threshold value of about 1150 ppmv, which is still consistent with the study of Manabe and Stouffer (1994).

## 5. Discussion

Our climate model includes only a limited subset of feedback mechanisms that are incorporated in three-dimensional models or that are relevant in the real climate system. Besides the low resolution and the limitation to only the deep ocean circulation, the model does not include the influence of land surfaces. Furthermore, atmospheric dynamics is absent and possible feedbacks due to a change in clouds have been neglected.

Although a thermodynamic sea ice model was included in the coupled model, no sea ice was formed in

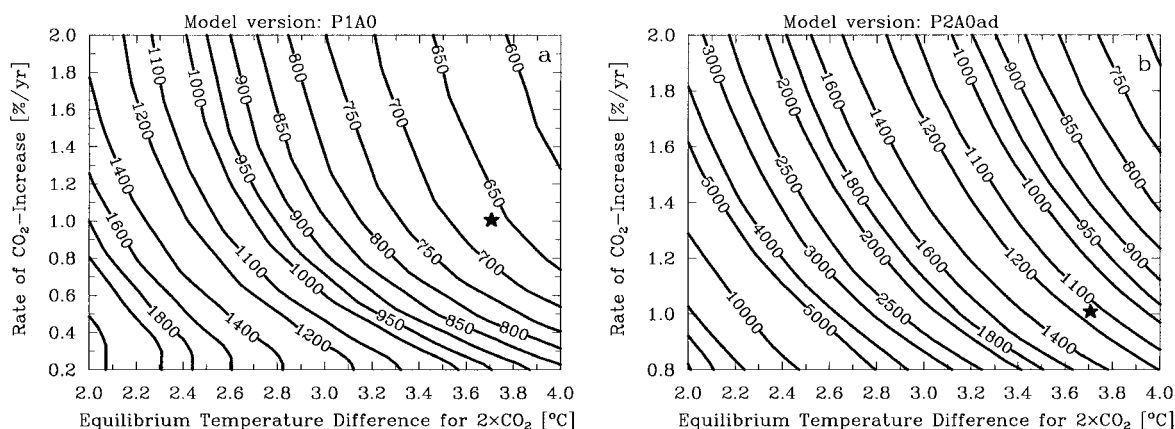


FIG. 21. Threshold concentration of atmospheric  $\text{CO}_2$  in ppmv beyond which the thermohaline circulation breaks down as a function of the equilibrium temperature rise for a doubling of  $\text{CO}_2$ ,  $\Delta T_{2\times}$ , and the rate of  $\text{CO}_2$  increase in percent per year. (a) Model version P1A0 (see Table 2). The experiments described in Fig. 5 have been performed for  $\Delta T_{2\times} = 3.7^\circ\text{C}$ ; for a  $\text{CO}_2$  increase of  $1\% \text{ yr}^{-1}$  the threshold lies between 650 and 700 ppmv in this model version (denoted by  $\star$ , from Stocker and Schmittner 1997). (b) Model version P2A0ad; no model runs were performed for rates smaller than  $0.8\% \text{ yr}^{-1}$ .

any of the present experiments. This is because neither the seasonal cycle nor the Arctic basin is included. Former studies showed that sea ice can form if the thermohaline circulation of the North Atlantic breaks down (Wright and Stocker 1993). Although the circulation shuts down also in the present experiments (e.g., expt. 750), the superimposed warming keeps the sea surface from freezing. In similar experiments some three-dimensional models predict the maximum warming at high northern latitudes, because the Arctic sea ice retreats (Manabe and Stouffer 1994; Cubasch et al. 1992). Since we do not predict sea ice in the Arctic Ocean, we can only crudely account for this positive feedback through a simple ice-albedo parameterization. The potential contribution of melting sea ice to the freshwater input into the North Atlantic, on the other hand, appears to be negligible (Manabe and Stouffer, 1994).

Changes in the atmospheric circulation, especially changes of the zonal winds, are not considered here. These would influence the gyre circulation of the upper ocean and the vertical exchange in the near surface due to the Ekman circulation with an associated stabilizing effect on the thermohaline circulation as reported by Fanning and Weaver (1997).

On the other hand, many basic feedback mechanisms are incorporated in the zonally averaged model. For example, there is positive feedback between the thermohaline circulation and the poleward atmospheric moisture transport or the ice-albedo feedback. Advantages of the model are its computational efficiency and the absence of flux corrections. These must be applied by most coupled three-dimensional models in order to avoid a drift into an unrealistic climate state after coupling the ocean with the atmosphere. The use of flux corrections is based on a linearization of the errors of the ocean-atmosphere exchange fluxes (Sausen et al. 1988) and is therefore only applicable for small, linear

deviations from the modern state of climate (Cubasch et al. 1994). The profound, nonlinear changes that the climate system experiences in the case when the thermohaline circulation breaks down violate this assumption (Egger 1995).

## 6. Conclusions

Global warming experiments with a simplified coupled ocean-atmosphere model have been performed. Despite the simplicity of the model many features of three-dimensional climate model responses to the radiative forcing are reproduced here. In particular, the existence of threshold values for atmospheric  $\text{CO}_2$ -equivalent greenhouse gases beyond which the Atlantic deep water formation stops is in qualitative and quantitative agreement with three-dimensional coupled models. We showed that these threshold values also depend on the rate of  $\text{CO}_2$  increase. A slower increase leads to higher threshold concentrations.

Furthermore, we examined the influence of the hydrological cycle on the model response. A variable meridional water vapor flux is crucial for the existence of realistic threshold values and responsible for a stronger temperature increase at high latitudes.

The inclusion of a simple ice-albedo feedback parameterization further enhances the warming at high latitudes and increases the sensitivity of the model. Sensitivity studies were performed for a range of climate sensitivities and rates of  $\text{CO}_2$  increase. These experiments were done for different parameterizations of the zonal distribution of precipitation and for model versions with and without a simple ice-albedo parameterization to examine a possible range of threshold concentrations of  $\text{CO}_2$  beyond which the thermohaline circulation breaks down. Additionally, the influence of localized negative diffusivities was investigated. The

zonal distribution of precipitation as well as the inclusion of an advective water vapor transport have considerable impact on the CO<sub>2</sub>-threshold concentration values.

In order to perform more realistic global warming simulations, the different formulations of the hydrological cycle presented here should be validated with observations in the future. The inclusion of the prescribed atmospheric CO<sub>2</sub> concentrations from the beginning of the industrialization until now ("cold-start correction"), as well as the inclusion of a marine carbon cycle (Marchal et al. 1998), should be utilized to perform more realistic global warming experiments with emission scenarios as model input instead of the prescribed atmospheric CO<sub>2</sub> concentration. Additionally, it is desirable that some experiments with different rates of increase of greenhouse gases and their influence on the thermohaline circulation should be redone with state-of-the-art three-dimensional ocean-atmosphere models in order to examine the threshold values with more quantitative confidence.

Calculations of emission scenarios (Houghton et al. 1996) and estimates of future oceanic uptake of anthropogenic CO<sub>2</sub> rely on the assumption of a steady-state carbon cycle. The findings presented here show that the ventilation of the deep ocean could be substantially reduced in the future. The dependency of the magnitude of this reduction on the emission rates will possibly have implications on a particular choice of a future emission scenario.

**Acknowledgments.** This study was supported by the Swiss National Science Foundation and partly by the Swiss Priority Programme Environment through module CLEAR2. We thank two anonymous reviewers for their comments that improved the paper.

#### REFERENCES

- Arrhenius, S., 1896: On the influence of carbonic acid in the air upon the temperature of the ground. *Philos. Mag.*, **41**, 237–276.
- Broecker, W. S., and G. H. Denton, 1989: The role of ocean-atmosphere reorganizations in glacial cycles. *Geochim. Cosmochim. Acta*, **53**, 2465–2501.
- , D. Peteet, and D. Rind, 1985: Does the ocean-atmosphere system have more than one stable mode of operation? *Nature*, **315**, 21–25.
- Bryan, F., 1986: High-latitude salinity effects and interhemispheric thermohaline circulations. *Nature*, **323**, 301–304.
- Chen, D., R. Gerdes, and G. Lohmann, 1995: A 1-D atmospheric energy balance model developed for ocean modelling. *Theor. Appl. Climatol.*, **51**, 25–38.
- Crowley, T. J., 1992: North Atlantic deep water cools the Southern Hemisphere. *Paleoceanography*, **7** (4), 489–497.
- , and G. R. North, 1991: *Paleoclimatology*. Oxford Monogr. on Geol. and Geophys., No. 18, Oxford University Press, 16 pp.
- Cubasch, U., K. Hasselmann, H. Hoeck, E. Maier-Reimer, U. Mikolajewicz, B. D. Santer, and R. Sausen, 1992: Time-dependent greenhouse warming computations with a coupled ocean-atmosphere model. *Climate Dyn.*, **8**, 55–69.
- , B. D. Santer, A. Hellbach, G. Hegerl, H. Hoeck, E. Maier-Reimer, U. Mikolajewicz, A. Stössel, and R. Voss, 1994: Monte Carlo climate change forecasts with a global coupled ocean-atmosphere model. *Climate Dyn.*, **10**, 1–19.
- , G. C. Hegerl, A. Hellbach, H. Hoeck, U. Mikolajewicz, B. D. Santer, and R. Voss, 1995: A climate change simulation starting 1935. *Climate Dyn.*, **11**, 71–84.
- Egger, J., 1995: Flux correction: Tests with a simple ocean-atmosphere model. *Climate Dyn.*, **13**, 285–292.
- Fanning, A. F., and A. J. Weaver, 1996: An atmospheric energy-moisture balance model: Climatology, interpentadal climate change, and coupling to an oceanic general circulation model. *J. Geophys. Res.*, **101**, 15 111–15 128.
- , and —, 1997: Temporal-geographical meltwater influences on the North Atlantic conveyor: Implications for the Younger Dryas. *Paleoceanography*, **12**, 307–320.
- Fourier, J.-B. J., 1824: Remarques générales sur les températures du globe terrestre et des espaces planétaires. *Ann. Chim. Phys.*, **27**, 136–167.
- Ghil, M., 1976: Climate stability for a Sellers-type model. *J. Atmos. Sci.*, **33**, 3–20.
- , 1985: Theoretical climate dynamics: An introduction. *Turbulence and Predictability in Geophysical Fluid Dynamics and Climate Dynamics*, M. Ghil, Ed., North-Holland, 347–402.
- Gill, A. E., 1982: *Atmosphere-Ocean Dynamics*. International Geophysics Series, Vol. 30, Academic Press, 662 pp.
- Gregory, J. M., and J. F. B. Mitchell, 1997: The climate response to CO<sub>2</sub> of the Hadley Centre coupled AOGCM with and without flux adjustment. *Geophys. Res. Lett.*, **24**, 1943–1946.
- Harvey, L. D. D., 1988: A semianalytic energy balance climate model with explicit sea ice and snow physics. *J. Climate*, **1**, 1065–1084.
- Houghton, J. T., L. G. Meira Filho, B. A. Callander, N. Harris, A. Kattenberg, and K. Maskell, Eds., 1996: *Climate Change 1995: The Science of Climate Change*. Cambridge University Press, 285 pp.
- James, I. N., 1994: *Introduction to Circulating Atmospheres*. Cambridge University Press, 246 pp.
- Keeling, C. D., and T. P. Whorf, 1994: Atmospheric CO<sub>2</sub> records from sites in the SIO network. *Trends '93: A Compendium of Data on Global Change*, T. Boden, D. Kaiser, R. Sepanski, and F. Stoss, Eds., Carbon Dioxide Information Analysis Center, 16–26.
- Levitus, S., 1982: *Climatological Atlas of the World Ocean*. NOAA Prof. Paper 13, U.S. Government Printing Office, Washington, DC, 173 pp.
- , and T. P. Boyer, 1994: *NOAA Atlas NESDIS 4, World Ocean Atlas 1994*. Vol. 4, *Temperature*, U.S. Department of Commerce, 117 pp.
- , R. Burgett, and T. P. Boyer, 1994: *NOAA Atlas NESDIS 3, World Ocean Atlas 1994*. Vol. 3, *Salinity*, U.S. Department of Commerce, 99 pp.
- Lorenz, E. N., 1979: Forced and free variations of weather and climate. *J. Atmos. Sci.*, **36**, 1367–1376.
- Manabe, S., and R. J. Stouffer, 1988: Two stable equilibria of a coupled ocean-atmosphere model. *J. Climate*, **1**, 841–866.
- , and —, 1993: Century-scale effects of increased atmospheric CO<sub>2</sub> on the ocean-atmosphere system. *Nature*, **364**, 215–218.
- , and —, 1994: Multiple-century response of a coupled ocean-atmosphere model to an increase of atmospheric carbon dioxide. *J. Climate*, **7**, 5–23.
- , M. J. Spelman, and K. Bryan, 1991: Transient responses of a coupled ocean-atmosphere model to gradual changes of atmospheric CO<sub>2</sub>. *J. Climate*, **4**, 785–818.
- Marchal, O., T. F. Stocker, and F. Joos, 1998: A latitude-depth, circulation-biogeochemical ocean model for paleoclimate studies: Development and sensitivities. *Tellus*, **50B**, 290–316.
- Nefel, A., H. Oeschger, T. Staffellbach, and B. Stauffer, 1988: CO<sub>2</sub> record in the Byrd ice core 50,000–5,000 years BP. *Nature*, **331**, 609–611.
- Oeschger, H., J. Beer, U. Siegenthaler, B. Stauffer, W. Dansgaard, and C. C. Langway, 1984: Late glacial climate history from ice

- cores. *Climate Processes and Climate Sensitivity*, *Geophys. Monogr.*, No. 29, Amer. Geophys. Union, 299–306.
- Oort, A. H., 1983: Global atmosphere circulation statistics, 1958–1973. NOAA Prof. Paper 14, U.S. Government Printing Office, Washington, DC, 180 pp.
- Peixoto, J. P., and A. H. Oort, 1992: *Physics of Climate*. American Institute of Physics, 195 pp.
- Rahmstorf, S., J. Marotzke, and J. Willebrand, 1996: Stability of the thermohaline circulation. *The Warmwatersphere of the North Atlantic Ocean*, W. Krauss, Ed., Gebrüder Borntraeger, 129–158.
- Revelle, R., 1985: The scientific history of carbon dioxide. *The Carbon Cycle and Atmospheric CO<sub>2</sub>: Natural Variations Archean to Present*, *Geophys. Monogr.*, No. 32, Amer. Geophys. Union, 1–4.
- Sausen, R., K. Barthel, and K. Hasselmann, 1988: Coupled ocean–atmosphere models with flux correction. *Climate Dyn.*, **2**, 145–163.
- Sellers, W. D., 1969: A global climate model based on the energy balance of the earth–atmosphere system. *J. Appl. Meteor.*, **8**, 392–400.
- Shine, K. P., R. G. Derwent, D. J. Wuebbles, and J.-J. Morcrette, 1995: Radiative forcing of climate. *Climate Change: The IPCC Scientific Assessment*, J. Y. Houghton, G. J. Jenkins, and J. J. Ephraums, Eds., Cambridge University Press, 41–68.
- Stephens, G. L., G. G. Campbell, and T. H. von der Haar, 1981: Earth radiation budgets. *J. Geophys. Res.*, **86**, 9739–9760.
- Stocker, T. F., and D. G. Wright, 1996: Rapid changes in ocean circulation and atmospheric radiocarbon. *Paleoceanography*, **11**, 773–796.
- , and A. Schmittner, 1997: Influence of CO<sub>2</sub> emission rates on the stability of the thermohaline circulation. *Nature*, **388**, 862–865.
- , D. G. Wright, and L. A. Mysak, 1992: A zonally averaged, coupled ocean–atmosphere model for paleoclimate studies. *J. Climate*, **5**, 773–797.
- Syktus, J., J. Chappel, R. Oglesby, J. Larson, S. Marshall, and B. Saltzman, 1997: Latitudinal dependence of signal-to-noise patterns from two general circulation models with CO<sub>2</sub> forcing. *Climate Dyn.*, **13**, 293–302.
- Wright, D. G., and T. F. Stocker, 1991: A zonally averaged ocean model for the thermohaline circulation. Part I: Model development and flow dynamics. *J. Phys. Oceanogr.*, **21**, 1713–1724.
- , and —, 1993: Younger Dryas experiments. *Ice in the Climate System*, W. R. Peltier, Ed., NATO ASI Series, Vol. 12, Springer-Verlag, 395–416.
- , —, and D. Mercer, 1998: Closures used in zonally averaged ocean models. *J. Phys. Oceanogr.*, **28**, 791–804.